Superconducting and normal-state properties of the layered boride OsB$_2$

Yogesh Singh, A. Niazi, M. D. Vannette, R. Prozorov, and D. C. Johnston

Ames Laboratory and Department of Physics and Astronomy, Iowa State University, Ames, Iowa 50011, USA

OsB$_2$ crystallizes in an orthorhombic structure (*Pmmn*) which contains alternate boron and osmium layers stacked along the *c* axis. The boron layers consist of puckered hexagons as opposed to the flat graphite-like boron layers in MgB$_2$. OsB$_2$ is reported to become superconducting below 2.1 K. We report results of the dynamic and static magnetic susceptibilities, electrical resistivity, Hall effect, heat capacity, and penetration depth measurements on arc-melted polycrystalline samples of OsB$_2$ to characterize its superconducting and normal-state properties. These measurements confirmed that OsB$_2$ becomes a bulk superconductor below T_c = 2.1 K. Our results indicate that OsB$_2$ is a moderate-coupling type-II superconductor with an electron-phonon coupling constant $\lambda_{ep} \approx 0.4 - 0.5$, a small Ginzburg-Landau parameter $\kappa \sim 1 - 2$, and an upper critical magnetic field $H_{c2}(0.5 \text{ K}) \sim 420$ Oe for an unannealed sample and $H_{c2}(1 \text{ K}) \sim 330$ Oe for an annealed sample. The temperature dependence of the superfluid density $n_s(T)$ for the unannealed sample is consistent with an *s*-wave superconductor with a slightly enhanced zero temperature gap $\Delta(0) = 1.9k_BT_c$ and a zero temperature London penetration depth $\lambda(0) = 0.38(2)$ μm. The $n_s(T)$ data for the annealed sample show deviations from the predictions of the single-band *s*-wave BCS model. The magnetic, transport, and thermal properties in the normal state of isostructural and isoelectronic RuB$_2$, which is reported to become superconducting below 1.6 K, are also reported.

I. INTRODUCTION

Since the discovery of superconductivity in MgB$_2$ at a remarkably high temperature $T_c \approx 39$ K,[1] there has been a renewed interest in the study of metal diborides. Many structurally related TB$_2$ compounds (T=Ti, Zr, Hf, V, Cr, Nb, Ta, and Mo) have been investigated in the search for superconductivity,[2–4] some of which had already been studied in the past.[5]

Among all binary diborides with the AlB$_2$ structure, apart from MgB$_2$, superconductivity has only been reported for ZrB$_2$ ($T_c \approx 5.5$ K),[3] NbB$_2$ ($T_c \approx 0.6$ K), Zr$_{0.13}$Mo$_{0.87}$B$_2$ ($T_c \approx 5$ K),[5] and TaB$_2$ ($T_c \approx 10$ K) (Ref. [2]) although there are controversies about superconductivity in ZrB$_2$, NbB$_2$, and TaB$_2$.[3,4] It has been argued using band structure calculations that in MgB$_2$, the high T_c is due to the B $2p$ bands at the Fermi energy, and that any chemical, structural, or other influence that changes this depresses T_c.[6] OsB$_2$ and RuB$_2$, which form in an orthorhombic structure (*Pmmn*) containing deformed boron sheets instead of a planar boron array as in MgB$_2$, have also been reported to become superconducting below 2.1 and 1.6 K, respectively.[7] Recently, the bulk modulus of OsB$_2$ at ambient and high pressure and its hardness have been studied.[8] Other physical properties of OsB$_2$ besides T_c have not yet been reported. Band structure calculations suggest that OsB$_2$ and RuB$_2$ are indeed metallic.[9,10]

For comparison, the structures of MgB$_2$ and OsB$_2$ are shown in Fig. 1. While MgB$_2$ has flat graphite-like sheets of boron separated by a layer of transition metal atoms in a hexagonal close packing arrangement [Fig. 1(a)],[1] the OsB$_2$ structure has sheets of a deformed two-dimensional network of corrugated boron hexagons. The boron layers lie between two planar transition metal layers which are offset [Fig. 1(b)].[9]

Herein, we report the dynamic and static magnetic susceptibilities, specific heat, resistivity, Hall effect, and pen-
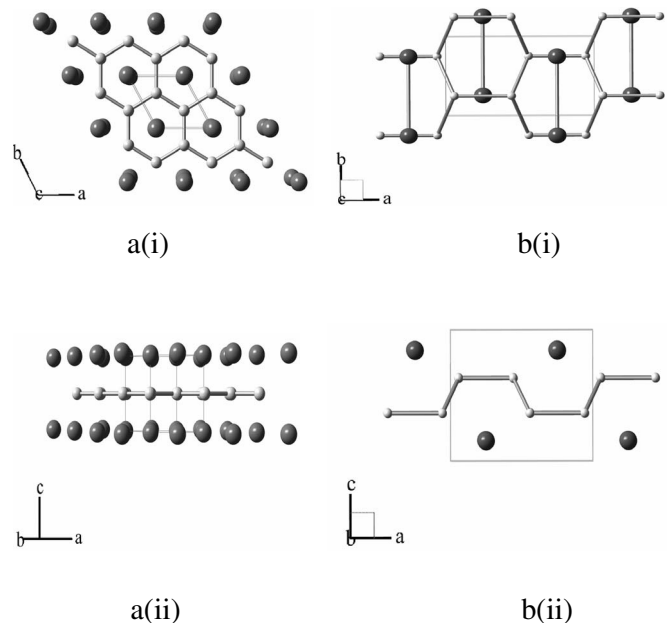

FIG. 1. The crystal structures of (a) MgB$_2$ and (b) OsB$_2$. The transition metal atoms are shown as large spheres, while the boron atoms are shown as small spheres. a(i) The MgB$_2$ structure viewed along the *c* axis and a(ii) perpendicular to the *c* axis. The MgB$_2$ structure has alternate boron and transition metal planes stacked along the *c* axis. The boron atoms form graphite-like sheets in the *ab* plane separated by a layer of transition metal atoms in a hexagonal close packing arrangement (Ref. [1]). b(i) The OsB$_2$ structure viewed along the *c* axis and b(ii) viewed perpendicular to the *c* axis. The OsB$_2$ structure has a deformed two-dimensional network of corrugated boron hexagon sheets. Along the *c* axis, the boron layers lie between two planar transition metal layers which are offset along the *ab* plane (Ref. [9]).

etration depth studies on OsB_2 to characterize its superconducting and normal-state properties. We confirmed that OsB_2 is metallic and becomes superconducting below $T_c = 2.1$ K. Our results indicate that OsB_2 is a moderate-coupling superconductor with an electron-phonon coupling constant $\lambda_{ep} \approx 0.4$–0.5, a small Ginzburg-Landau parameter $\kappa \sim 1$–2, and an upper critical magnetic field $H_{c2}(0.5 \text{ K}) \sim 420$ Oe for an unannealed sample and $H_{c2}(1 \text{ K}) \sim 330$ Oe for an annealed sample. We also report measurements on RuB_2 which show similar normal-state properties. The paper is organized as follows. Experimental details are given in Sec. II. The structural results are presented in Sec. III A. The normal-state electrical resistivity, magnetic susceptibility, and heat capacity data for the unannealed OsB_2 and RuB_2 samples are given in Sec. III B 1 and their superconducting properties are presented in Sec. III B 2. The normal-state and superconducting properties of the annealed OsB_2 sample are presented in Sec. III C. The paper is concluded in Sec. IV.

II. EXPERIMENTAL DETAILS

The binary phase diagram of the Os-B system has recently been investigated in detail and it has been shown that OsB_2 melts congruently at about 1870 °C.[11] Polycrystalline samples (~ 1 g) of OsB_2 used in this study were therefore prepared by arc melting. The two OsB_2 samples for which the properties are reported here were prepared with starting materials of different purities. One sample (sample A) was prepared from Os powder (99.95%, Alfa Aesar) and B chunks (99.5%, Alfa Aesar). The magnetization of this sample showed the presence of a large amount of paramagnetic impurities as apparent in the low-temperature measurements. Therefore, another sample of OsB_2 (sample B) was prepared using ultrahigh purity Os (99.995%, Sigma Aldrich) and ^{11}B (99.999%, Eagle Pitcher). The magnetization for this sample showed that the concentration of paramagnetic impurities was considerably reduced compared to the first sample. The superconducting transition temperature and transition width are similar for these two samples. Most of the measurements pertaining to the superconducting state have been done on sample A, while sample B has been used to obtain the intrinsic magnetic susceptibility of OsB_2 and for ^{11}B NMR measurements, which have been reported elsewhere.[12]

The samples were prepared as follows. The constituent elements were taken in stoichiometric proportion and arc-melted on a water-cooled copper hearth in high purity argon atmosphere. A Zr button was used as an oxygen getter. The sample was flipped over and remelted 10–15 times to ensure homogeneous mixing of the constituent elements. The mass of the ingot was checked after the initial two meltings, and any weight loss due to the shattering of boron during melting was compensated by adding the appropriate amount of boron in subsequent melts. The arc-melted ingot so obtained had a shiny metallic luster with well formed crystal facets on the surface. A part of sample A was wrapped in Zr foil and annealed for ten days at 1150 °C in a sealed quartz tube. A sample of the isostructural compound RuB_2 was prepared similarly from high purity Ru powder (99.995%, MV labs) and ^{11}B (99.999%, Eagle Pitcher). A portion of the as-cast

samples was crushed for powder x-ray diffraction. Powder x-ray diffraction (XRD) patterns were obtained using a Rigaku Geigerflex diffractometer with Cu $K\alpha$ radiation, in the 2θ range from 10° to 90° with a 0.02° step size. Intensity data were accumulated for 5 s per step.

Samples of starting composition $OsB_{1.9}$ and $OsB_{2.1}$ were also prepared with the above starting materials from Alfa Aesar. Powder x-ray diffraction measurements on crushed pieces of these samples showed that $OsB_{1.9}$ is a two-phase sample containing the phases Os_2B_3 and OsB_2, while the $OsB_{2.1}$ sample contained the phase OsB_2 and elemental osmium. The purpose of making these samples was to explore both the boron-deficient and boron-rich sides, respectively, of the homogeneity range of OsB_2, if any, and its influence on the superconducting properties.

The temperature dependence of the dc magnetic susceptibility and isothermal magnetization was measured using a commercial superconducting quantum interference device (SQUID) magnetometer (MPMS5, Quantum Design). The resistivity and heat capacity were measured using a commercial Physical Property Measurement System (PPMS, Quantum Design). The magnetic susceptibility measurements were done on samples of arbitrary shape. The magnetization M versus field H measurements in Figs. 9 and 16 below were performed on a parallelepiped sample with the following dimensions: length=3.25 mm, width=1.57 mm, and thickness=0.35 mm, with the magnetic field applied parallel to the length of the sample to minimize demagnetization effects. The $M(H)$ loops in Figs. 10 and 16 below were measured with the field applied either parallel or perpendicular to the length of the sample. The resistance was measured using a four-probe technique with an ac current of 5 mA along the long axis of the rectangular bar, corresponding to a current density of 0.91 A/cm^2.

The dynamic susceptibility was measured between 0.5 and 2.5 K using a 10 MHz tunnel-diode driven oscillator (TDO) circuit with a volume susceptibility sensitivity $\Delta \chi \approx 10^{-8}$.[13] For superconductors, this is equivalent to a change in the London penetration depth of about 0.5 Å for millimeter-sized samples.[13–15] A TDO is an LC tank circuit with a coil of inductance L and a capacitor C. The circuit is self-resonating at a frequency $2\pi f = 1/\sqrt{LC}$. When a sample with susceptibility χ is inserted into the coil, the total inductance decreases for a diamagnetic sample or increases for a paramagnetic sample. The resonant frequency changes accordingly by an amount which is proportional to χ.[13] Specifically, the device measures the temperature dependence of the resonant frequency shift $\Delta f(T)$ induced by changes in the sample's magnetic response. The magnetic susceptibility χ is then given by[15]

$$\Delta f(T) = -4\pi \chi(T) G \approx -G \left[1 - \frac{\lambda(T)}{R} \tanh\left(\frac{R}{\lambda(T)} \right) \right], \quad (1)$$

where G is a sample-shape- and coil-dependent calibration parameter, R is the effective sample dimension, and $\lambda(T)$ is the London penetration depth. G has been determined by matching the temperature dependence of the skin depth ob-
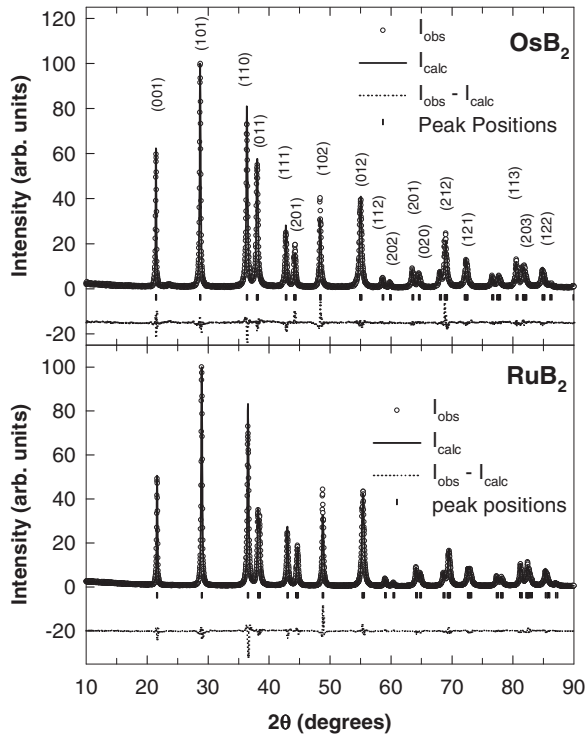
FIG. 2. Rietveld refinements of the OsB_2 and RuB_2 x-ray diffraction data. The open symbols represent the observed x-ray pattern, the solid lines represent the fitted pattern, the dotted lines represent the difference between the observed and calculated intensities, and the vertical bars represent the peak positions.

tained from the resonator response in the normal state of OsB_2 to the measured resistivity data.

III. RESULTS

A. Structures of OsB_2 and RuB_2

All the lines in the x-ray patterns for OsB_2 and RuB_2 could be indexed to the known orthorhombic *Pmmn* (No. 59) structure, and Rietveld refinements,[16] shown in Fig. 2, of the x-ray patterns gave the lattice parameters $a=4.6851(6)$ Å, $b=2.8734(4)$ Å, and $c=4.0771(5)$ Å for OsB_2 and $a=4.6457(5)$ Å, $b=2.8657(3)$ Å, and $c=4.0462(4)$ Å for RuB_2. These values are in excellent agreement with previously reported values.[17] The best fits were obtained when the
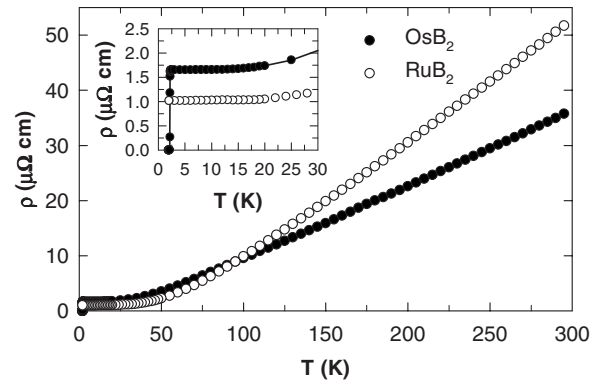

FIG. 3. Electrical resistivity ρ for OsB_2 and RuB_2 versus temperature T. The inset shows the low-temperature data on an expanded scale to highlight the low residual resistivity.

anisotropic thermal parameters for the transition metal atom were allowed to vary. For boron, the overall isotropic thermal parameter was fixed to zero because unphysically large values were obtained when it was allowed to vary, and fixing it to zero did not change the quality of the fit. This is probably because the atomic number of boron is much less than that of either Os or Ru. A neutron diffraction study is needed to obtain reliable estimates of the thermal parameters for boron. Some parameters obtained from the Rietveld refinement are given in Table I. Although the lattice parameters and fractional atomic positions that we obtained from the Rietveld refinements for both OsB_2 and RuB_2 agree reasonably well with the earlier structural report,[17] the fits consistently underestimate the intensities of the (102) peaks at $2\theta = 48.35°$ (see Fig. 2).

B. Unannealed samples

1. Normal-state properties of OsB_2 and RuB_2

The electrical resistivity (ρ) versus temperature of OsB_2 (sample A) and RuB_2 from 1.75 to 300 K is shown in Fig. 3. The room temperature resistivity values are 36(3) $\mu\Omega$ cm for OsB_2 and 53(5) $\mu\Omega$ cm for RuB_2. The error in the resistivity comes primarily from the error in the determination of the geometrical factors. Both compounds show metallic behavior with an approximately linear decrease in resistivity on cooling from room temperature. At low temperatures, ρ becomes

TABLE I. Structure parameters for OsB_2 and RuB_2 refined from powder XRD data. B_{11}, B_{22}, and B_{33} are the anisotropic thermal parameters defined within the thermal parameter of the intensity as $e^{-(B_{11}h^2+B_{22}k^2+B_{33}l^2)/\lambda^2}$.

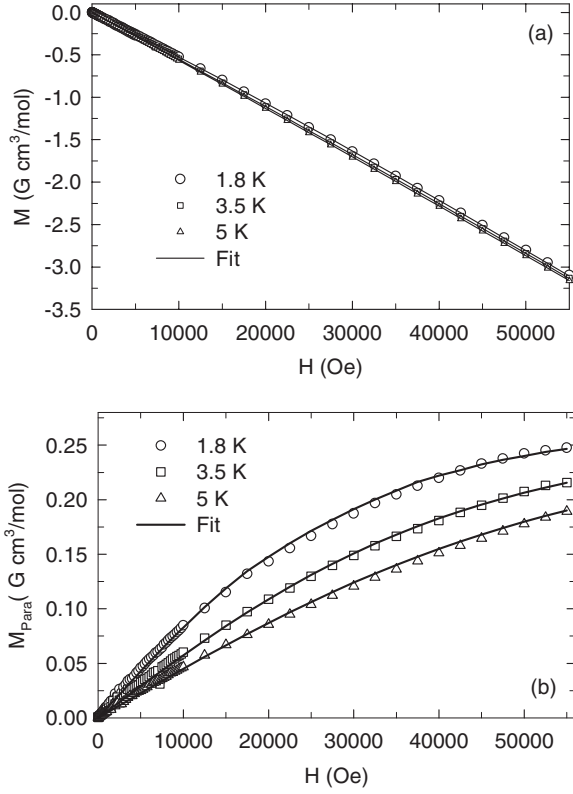| Sample	Atom	x	y	z	B_{11} (Å^2)	B_{22} (Å^2)	B_{33} (Å^2)	R_{wp}/R_p
OsB_2	Os	0.25	0.25	0.1515(3)	0.0209(9)	0.045(2)	0.001(1)	1.39
	B	0.093(3)	0.25	0.669(4)				
RuB_2	Ru	0.25	0.25	0.1490(2)	0.0166(7)	0.051(2)	0.0007(9)	1.36
	B	0.063(1)	0.25	0.638(2)				

FIG. 4. (a) The magnetization M versus applied magnetic field H for OsB_2 (sample B). The solid curves are fits by Eq. (2). (b) The paramagnetic impurity contribution M_{Para} to the total $M(H)$. The solid curves are the paramagnetic impurity part of Eq. (2).

only weakly temperature dependent and reaches a residual resistivity ρ_0 of 1.7(2) $\mu\Omega$ cm just above 2.2 K for OsB_2 and 1.1(1) $\mu\Omega$ cm at 1.8 K for RuB_2 as seen in the inset of Fig. 3. The large residual resistivity ratios RRR$=\rho(300$ K$)/\rho_0$ $=22$ for OsB_2 and RRR$=51$ for RuB_2 indicate well-crystallized homogeneous samples. For OsB_2, the resistivity drops abruptly below 2.2 K and reaches zero by 2.14 K, as highlighted in the inset of Fig. 3. The superconducting properties will be discussed in detail in Sec. III B 2.

Both OsB_2 and RuB_2 are so weakly magnetic that even trace amounts (a few ppm) of magnetic impurities are apparent in the low-temperature susceptibility and magnetization $M(H)$ measurements. The $M(H)$ data for OsB_2 at 1.8, 3.5, and 5 K are shown in Fig. 4(a). The data were fitted by the expression

$$M(H) = \chi_0 H + fN_A g S \mu_B B_S(x) \equiv \chi_0 H + M_{Para}(H), \quad (2)$$

where χ_0 is the intrinsic susceptibility of OsB_2, f is the molar fraction of paramagnetic impurities, N_A is Avogadro's number, g is the g-factor of the impurity spins, S is the spin of the paramagnetic impurities, and $B_S(x)$ is the Brillouin function where the argument x of the Brillouin function is x $=g\mu_B S H/(T-\theta)$, where θ is the Weiss temperature. The g value was fixed to 2. The fitting parameters were χ_0, f, S, and θ, and we obtained $\chi_0=-6.09(1)\times10^{-5}$ cm^3/mol, f $=1.57(4)\times10^{-5}$, $S=1.54(6)$, and $\theta=-1.8(2)$ K. The fit is
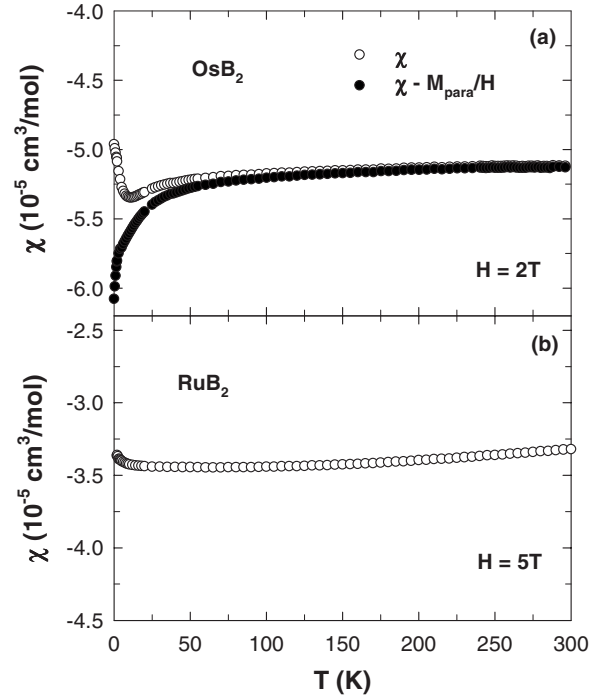

FIG. 5. Magnetic susceptibility χ (open circles) versus temperature T for (a) OsB_2 and (b) RuB_2. In (a), the filled circles are the values obtained after subtracting the paramagnetic impurity contribution (see text).

shown as the solid curves in Fig. 4(a). By subtracting from the observed $M(H)$ data the $\chi_0 H$ obtained from the fitting, one can obtain the contribution from paramagnetic impurities M_{Para} as shown in Fig. 4(b). The solid curves in Fig. 4(b) are the paramagnetic impurity part of the fit [the second term in Eq. (2)].

The normal-state susceptibility $\chi \equiv M/H$ for OsB_2 and RuB_2 has been measured versus temperature T between 1.8 and 300 K in fields of 2 and 5 T, respectively, as shown in Fig. 5 (the susceptibility of the sample holder was corrected for). The $\chi(T)$ for both samples is weakly temperature dependent between 50 and 300 K. For OsB_2, below 50 K, $\chi(T)$ drops somewhat on cooling, amounting to about 4% of the room temperature value. The upturn at low temperatures seen for both samples is most likely due to the presence of small amounts (a few ppm) of paramagnetic impurities as determined above for OsB_2 ($f=16$ molar ppm). Figure 5(a) also shows the susceptibility of OsB_2 after subtracting the paramagnetic impurity contribution $\chi_{Para}=M_{Para}/H$ from the observed χ.

The intrinsic susceptibility after subtracting χ_{Para}, $\chi(T)$, can be written as

$$\chi = \chi_{core} + \chi_L + \chi_{VV} + \chi_P, \quad (3)$$

where χ_{core} is the diamagnetic orbital contribution from the electrons (ionic or atomic), χ_L is the Landau orbital diamagnetism of the conduction electrons, χ_{VV} is the Van Vleck paramagnetic orbital contribution, and χ_P is the Pauli paramagnetic spin susceptibility of the conduction electrons. For

OsB_2 and RuB_2, the net diamagnetic susceptibility indicates quasi-free-electrons with $\chi_L = -\left(\frac{m}{m^*}\right)^2 \frac{\chi_P}{3}$ and $\chi_{VV} \approx 0$,[18] where m is the free electron mass and m^* is the effective mass of the current carriers. Assuming $m^* = m$, the Pauli susceptibility can be written as

$$\chi_P = \frac{3}{2}(\chi - \chi_{core}), \tag{4}$$

which can be extracted from the experimentally measured susceptibility, after correction for the paramagnetic impurity contribution, if the contribution from the core χ_{core} is known. In covalent metals, it is difficult to correctly estimate χ_{core} because its value depends on the local electron density on the atoms. In an ionic model, $\chi_{core} = -18 \times 10^{-6}$ cm^3/mol for Os^{6+} and -44×10^{-6} cm^3/mol for Os^{2+}.[19] However, if we use the ionic core diamagnetism values for Os and B, one obtains from Eq. (4) an unphysical negative χ_P. For OsB_2, it is reasonable to use atomic (covalent) estimates of χ_{core} instead of ionic values because the bonding in OsB_2 has a strong covalent character.[20] Therefore using the atomic diamagnetism values χ_{core} for Os (-53.82×10^{-6} cm^3/mol), Ru (-42.89×10^{-6} cm^3/mol), and B (-12.55×10^{-6} cm^3/mol),[21] we obtain $\chi_{core} = -78 \times 10^{-6}$ cm^3/mol for OsB_2 and $\chi_{core} = -68 \times 10^{-6}$ cm^3/mol for RuB_2. Subtracting these values and the paramagnetic impurity contribution from the total measured susceptibility and accounting for the Landau diamagnetism, one can get the Pauli paramagnetic susceptibility using Eq. (4), thus yielding $\chi_P = 2.7(3) \times 10^{-5}$ cm^3/mol at $T = 0$ K for OsB_2.

From χ_P, one can estimate the density of states at the Fermi level $N(\epsilon_F)$ for both spin directions using the relation

$$\chi_P = \mu_B^2 N(\epsilon_F), \tag{5}$$

where μ_B is the Bohr magneton. Taking the above $T = 0$ K value of χ_P for OsB_2, we get $N(\epsilon_F) = 1.7(2)$ states/eV f.u., where "f.u." means "formula unit." This value is larger than the value from band structure calculations [$N(\epsilon_F) \approx 0.55$ states/eV f.u.].[9] Similarly, from the average value of $\chi_P = 5.22(7) \times 10^{-5}$ cm^3/mol for RuB_2, one estimates, using Eq. (5), $N(\epsilon_F) = 3.0(2)$ states/eV f.u. This value is also larger than the value obtained from the band structure calculations [$N(\epsilon_F) \approx 0.53$ states/eV f.u.].[9] The discrepancy between experiment and theory for OsB_2 is discussed later in terms of the Stoner enhancement factor of the susceptibility.

Figure 6 shows the results of the normal-state heat capacity versus temperature $C(T)$ measurements on OsB_2 (sample A) and RuB_2, plotted as C versus T. The OsB_2 data were recorded in an applied magnetic field of 1 kOe to suppress the superconducting transition to below 1.75 K, which is the low-temperature limit of our measurements. The inset in Fig. 6 shows the low-temperature data for both samples plotted as C/T versus T^2. The low-temperature data (1.75–5 K) for both samples could be fitted by the expression $C = \gamma T + \beta T^3$, where the first term is the contribution from the conduction electrons and the second term is the contribution from the lattice. The fits are shown as the solid straight lines in the inset of Fig. 6. The values
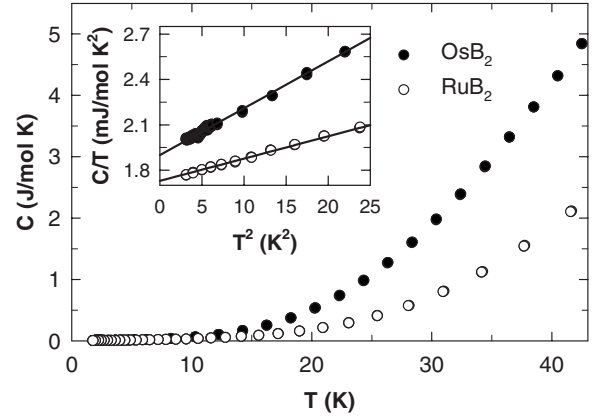

FIG. 6. The heat capacity C versus temperature T of OsB_2 and RuB_2 between 1.8 and 45 K. The inset shows the data plotted as C/T versus T^2 between 1.8 and 5 K. The solid straight lines are fits by the expression $C/T = \gamma + \beta T^2$.

$$\gamma = 1.90(1) \text{ mJ/mol K}^2 \quad \text{and} \quad \beta = 0.031(2) \text{ mJ/mol K}^4 \tag{6}$$

are obtained for OsB_2, and the values

$$\gamma = 1.72(3) \text{ mJ/mol K}^2 \quad \text{and} \quad \beta = 0.015(1) \text{ mJ/mol K}^4 \tag{7}$$

are obtained for RuB_2. From the values of β, one can obtain the Debye temperature Θ_D using the expression[22]

$$\Theta_D = \left(\frac{12\pi^4 R n}{5\beta}\right)^{1/3}, \tag{8}$$

where R is the molar gas constant and n is the number of atoms per f.u. ($n = 3$ for OsB_2 and RuB_2). We obtain $\Theta_D = 550(11)$ K for OsB_2 and $\Theta_D = 701(14)$ K for RuB_2. A simple harmonic oscillator model predicts $\Theta_D \propto \left(\frac{1}{M}\right)^{1/2}$,[22] where M is the molar mass of the compound. The ratio $\frac{\Theta_D(OsB_2)}{\Theta_D(RuB_2)} = 0.79(3)$ is indeed close to the square root of the ratio of the molar masses $\sqrt{\frac{M(RuB_2)}{M(OsB_2)}} = 0.76$.

Another quantity which characterizes a metal is the ratio of the density of states as probed by magnetic measurements to the density of states probed by heat capacity measurements, which is the Wilson ratio

$$R_W = \frac{\pi^2 k_B^2}{3\mu_B^2}\left(\frac{\chi_P}{\gamma}\right). \tag{9}$$

For a free-electron Fermi gas, $R_W = 1$. Using $\chi_P = 2.7(3) \times 10^{-5}$ cm^3/mol and $\gamma = 1.90(1)$ mJ/mol K^2 for OsB_2, we get $R_W = 1.03(2)$ at $T = 0$ K, which is of the order of unity expected for a quasi-free-electron gas. For RuB_2, $\chi_P = 5.22(7) \times 10^{-5}$ cm^3/mol and $\gamma = 1.72(3)$ mJ/mol K^2, which give $R_W = 2.21(7)$. Note that Eq. (9) is only valid for spin-1/2 particles if the electron-phonon interaction and the Stoner enhancement factor are negligible. If they are not, then one must use Eq. (13) below.
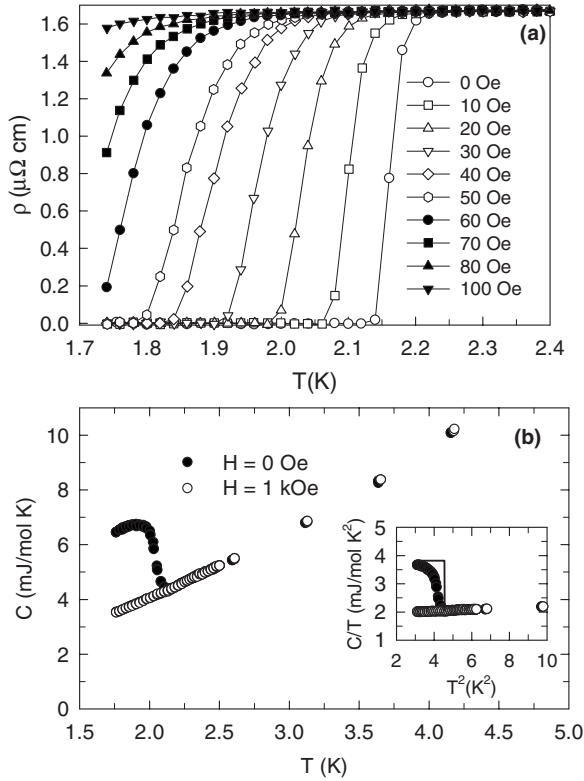
FIG. 7. (a) The resistivity $\rho(T)$ of OsB_2 between 1.7 and 2.4 K measured with various applied magnetic fields. (b) Temperature dependence of the heat capacity $C(T)$ of OsB_2 in zero and 1 kOe applied magnetic field. The inset shows the data plotted as C/T versus T^2. The solid line is a construction to estimate the magnitude of the superconducting anomaly (see text for details).

2. Superconducting properties of OsB₂

The results of the resistivity $\rho(T)$ and heat capacity $C(T)$ measurements at low temperatures are shown in Fig. 7 to highlight the superconducting transition. Figure 7(a) shows the low-temperature resistivity $\rho(T)$ data measured with various applied magnetic fields. In the zero-field data, there is an abrupt drop below 2.2 K and ρ reaches zero at T_c=2.14 K. The transition is quite sharp with a transition width (10%–90%) of approximately 40 mK. The superconducting transition is suppressed to lower temperatures in a magnetic field, as can be seen in Fig. 7(a). We will return to these data when we estimate the critical field.

Figure 7(b) shows the $C(T)$ data measured in zero and 1 kOe applied field. The sharp anomaly at 2.1 K seen in the heat capacity data taken in zero applied field confirms the bulk nature of the superconductivity in OsB_2. The transition is completely suppressed to below 1.7 K in 1 kOe as seen in Fig. 7(b). The inset in Fig. 7(b) shows the data plotted as C/T versus T^2. The jump in the specific heat ΔC at the superconducting transition T_c is usually normalized as $\Delta C/\gamma T_c$, where γ is the Sommerfeld coefficient. Since the anomaly at the superconducting transition is somewhat broad and the temperature range below T_c is insufficient, we estimate ΔC by constructing a transition at T_c with a ΔC equal to the maximum of the superconducting anomaly in C/T.

This is shown as the solid vertical line in the inset of Fig. 7(b). Using this value of $\Delta C/T_c$=1.78 mJ/mol K² and γ =1.90(1) mJ/mol K² obtained in the previous section, we get $\Delta C/\gamma T_c$=0.94. This is reduced from the value 1.43 expected from BCS theory. The origin of this suppression is not currently known. A reduced specific heat anomaly at the superconducting transition ($\Delta C/\gamma T_c \sim 1$) is also observed in the two-gap superconductor MgB_2.[23] To evaluate this question in OsB_2 requires $C(T)$ data to lower temperatures than in Fig. 7(b). However, we reiterate that the large specific heat jump at T_c demonstrates the bulk nature of the superconductivity in OsB_2.

We now estimate the electron-phonon coupling constant λ_{ep} using McMillan's formula,[24] which relates the superconducting transition temperature T_c to λ_{ep}, the Debye temperature Θ_D, and the Coulomb repulsion constant μ^*,

$$T_c = \frac{\Theta_D}{1.45} \exp\left[-\frac{1.04(1+\lambda_{ep})}{\lambda_{ep} - \mu^*(1+0.62\lambda_{ep})} \right], \quad (10)$$

which can be inverted to give λ_{ep} in terms of T_c, Θ_D, and μ^* as

$$\lambda_{ep} = \frac{1.04 + \mu^* \ln\left(\dfrac{\Theta_D}{1.45 T_c}\right)}{(1 - 0.62\mu^*)\ln\left(\dfrac{\Theta_D}{1.45 T_c}\right) - 1.04}. \quad (11)$$

From the above heat capacity measurements, we had obtained Θ_D=550(11) K, and using T_c=2.1 K, we get λ_{ep} =0.41 and 0.5 for μ^*=0.10 and 0.15, respectively. These values of λ_{ep} suggest that OsB_2 is a moderate-coupling superconductor (λ_{ep} for MgB_2 is ≈ 1).[25]

Having estimated λ_{ep}, the density of states at the Fermi energy for both spin directions $N(\epsilon_F)$ can be estimated from the values of γ and λ_{ep} using the relation[22]

$$\gamma = \frac{\pi^2}{6} k_B^2 N(\epsilon_F)(1 + \lambda_{ep}) \equiv \gamma_0(1 + \lambda_{ep}). \quad (12)$$

We find $N(\epsilon_F)$=1.14 and 1.06 states/eV f.u. for λ_{ep}=0.41 and 0.5, respectively. These values are larger than the value estimated by band structure calculations $N(\epsilon_F)$ $\approx$0.55 states/eV f.u.[9] The bare Sommerfeld coefficient with λ_{ep}=0.5 is γ_0=1.4 mJ/mol K².

One can now go back and reevaluate the Wilson ratio R_W. For a free electron Fermi gas, R_W=1. In Sec. III B 1, using the experimentally observed values of χ_P and γ, we had estimated R_W=1.03 for OsB_2. However, the electron-phonon interaction leads to an enhancement in γ from its value γ_0 in the absence of interactions, given by $\gamma=\gamma_0(1+\lambda_{ep})$. Similarly, electron-electron interactions lead to an enhancement in the Pauli susceptibility χ_P from its value χ_P^0 in the absence of interactions, given by $\chi_P = \frac{\chi_P^0}{1-\alpha}$, where α is the Stoner factor. The reevaluated Wilson ratio is then given by
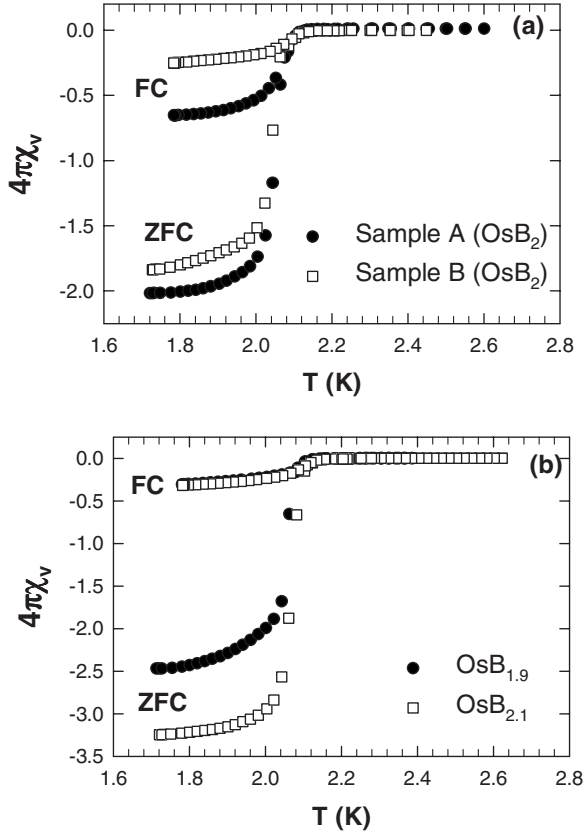
FIG. 8. Temperature T dependence of the zero-field-cooled (ZFC) and field-cooled (FC) volume susceptibility χ_v in terms of the superconducting volume fraction ($4\pi\chi_v$) of (a) OsB$_2$ (sample A and sample B) and (b) OsB$_{1.9}$ and OsB$_{2.1}$ in a field of 5 Oe from 1.7 K to 2.6 K.

$$R_W = \frac{\pi^2 k_B^2}{3\mu_B^2}\left(\frac{\chi_P^0}{\gamma_0}\right) = 1 = \frac{\pi^2 k_B^2}{3\mu_B^2}\left(\frac{\chi_P}{\gamma}\right)(1-\alpha)(1+\lambda_{ep}).$$

(13)

Using $\lambda_{ep}=0.41-0.5$ obtained in Sec. III B 1, one gets an estimate of the Stoner factor $\alpha=0.30-0.35$.

The temperature dependence of the zero-field-cooled (ZFC) and field-cooled (FC) dimensionless volume magnetic susceptibility χ_v of OsB$_2$ samples A and B in a field of 5 Oe from 1.7 to 2.8 K is plotted in Fig. 8(a), where $\chi_v=M_v/H$ and M_v is the volume magnetization. Complete diamagnetism corresponds to $\chi_v=-1/4\pi$, so the data have been normalized by $1/4\pi$. The data have not been corrected for the demagnetization factor N, which gives $\chi_v = \frac{-1/4\pi}{1-N}$ for the measured value. A sharp diamagnetic drop in the susceptibility below $T_c=2.14$ K for both samples signals the transition into the superconducting state. The width of the ZFC transition (10%–90% of the transition) is ≈ 95 mK for sample A and ≈ 80 mK for sample B.

In Fig. 8(b), the temperature dependence of the susceptibility of the samples with compositions OsB$_{1.9}$ and OsB$_{2.1}$ is shown. It can be seen that the onset temperature for the superconducting transition for both the samples is 2.1 K. This indicates that the homogeneity range of OsB$_2$, if any, does
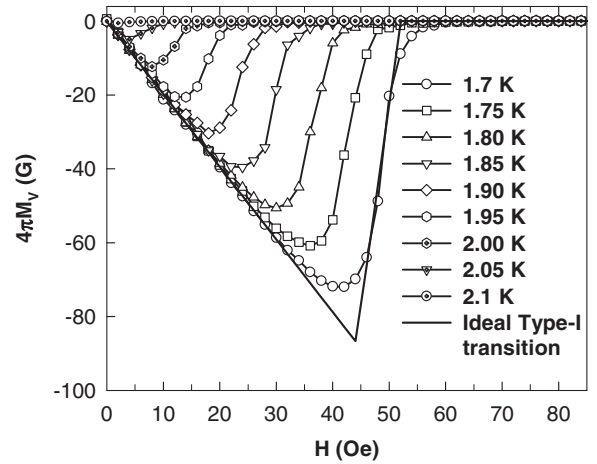

FIG. 9. Volume magnetization (M_v) normalized by $1/4\pi$, versus applied magnetic field (H) at various temperatures.

not have any significant effect on the T_c of OsB$_2$. All other measurements were therefore done on the single phase samples A and B of OsB$_2$.

To further characterize the superconducting state, we have performed measurements of the dc magnetization versus field $M(H)$ at various temperatures. The volume magnetization $M_v(H)$ normalized by $1/4\pi$ is shown in Fig. 9. The initial slope of the $M_v(H)$ curves is larger than the value -1 expected for perfect diamagnetism, which indicates nonzero demagnetization effects. The shape of the $M_v(H)$ curves in Fig. 9 for OsB$_2$ is suggestive of type-I superconductivity with demagnetization effects. The hysteretic $M_v(H)$ loops, shown in Figs. 10(a) and 10(b), were measured at 1.75 K with the magnetic field applied parallel and perpendicular, respectively, to the length of the sample as shown in the insets in Figs. 10(a) and 10(b). The sample is a parallelipiped with the following dimensions: length=3.25 mm, width =1.57 mm, and thickness=0.35 mm. There is a large irreversibility due to strong pinning in both measurements. We obtain an estimate of the reversible part of the magnetization M_{rev} by taking an average of the magnetization measured upon increasing and decreasing H between −100 and 100 Oe. The normalized M_{rev} obtained from the data in Fig. 10(a) is shown in Fig. 10(c) and M_{rev} obtained from the data in Fig. 10(b) is shown in Fig. 10(d). The data in Fig. 10(c) look like reversible magnetization curves for a type-I superconductor with demagnetization effects, similar to the data in Fig. 9 above. The data in Fig. 10(d) are too noisy to draw conclusions. However, additional measurements and analysis suggest instead that OsB$_2$ is a type-II superconductor (see below), with a Ginzburg-Landau parameter κ on the type-II side of the borderline between type-I and type-II superconductivity. The $M_v(H)$ in Figs. 9 and 10 are, however, quite different from those expected for a type-II superconductor,[26] an issue that needs to be addressed in future work.

From the $M_v(H)$ curves in Fig. 9, we have estimated the critical field $H_{c2}(T)$ from the construction in Fig. 9, illustrated for $T=1.7$ K. The $H_{c2}(T)$ has been determined by fitting a straight line to the data for a given temperature in the superconducting state and to the data in the normal state, and
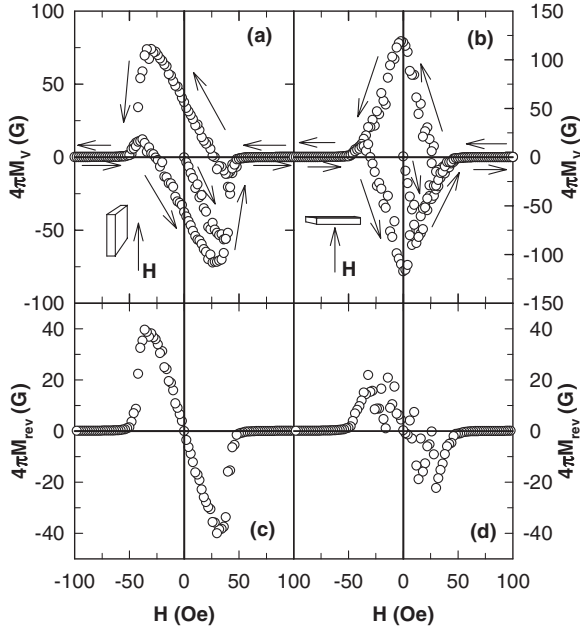
FIG. 10. (a) Hysteresis loop of the volume magnetization $M_v(H)$ normalized by $1/4\pi$, versus applied magnetic field H at 1.7 K. The magnetic field is applied parallel to the length of the sample as shown in the inset. The arrows next to the data indicate the direction of field ramping during the measurement. (b) Hysteresis loop of the volume magnetization $M_v(H)$ normalized by $1/4\pi$, versus applied magnetic field H at 1.7 K. The magnetic field is applied perpendicular to the length of the sample as shown in the inset. (c) The normalized reversible magnetization M_{rev} for the data shown in (a). (d) The normalized reversible magnetization M_{rev} for the data shown in (b).

taking the field H at which these lines intersect as the critical field at that temperature, $H_{c2}(T)$.

The dynamic ac susceptibility $\chi(T)$ data measured between 0.5 and 2.2 K at a frequency of 10 MHz in various applied magnetic fields are shown in Fig. 11. To determine $H_{c2}(T)$ from the data in Fig. 11, we have fitted a straight line to the data in the normal state and to the data below T_c for a
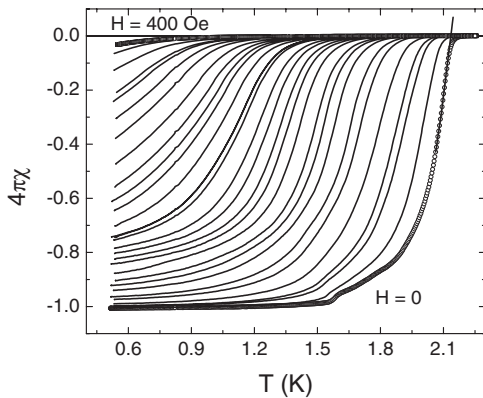

FIG. 11. Dynamic susceptibility χ normalized to $1/4\pi$, versus temperature T at a frequency of 10 MHz with various applied magnetic fields H. The data have been normalized to a minimum value of -1 at the lowest T.
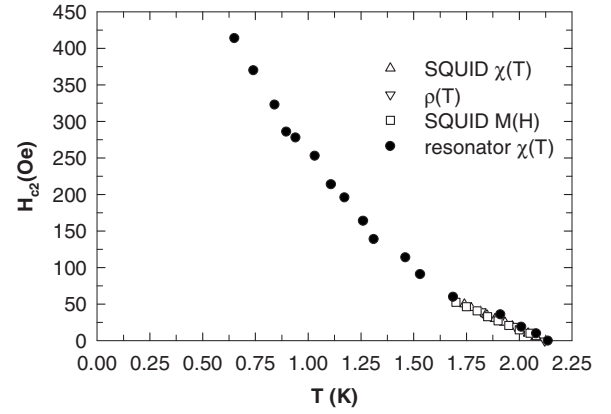

FIG. 12. Upper critical magnetic field H_{c2} versus temperature T extracted from four different types of measurements.

given applied magnetic field, and taken the value of T at which these lines intersect as $T_c(H)$. This is shown in Fig. 11 for the data at $H=0$. By inverting $T_c(H)$, we obtain $H_{c2}(T)$. H_{c2} has also been obtained in a similar way from the $\chi(T)$ $\equiv M(T)/H$ SQUID magnetometer data (not shown here) between 1.7 and 2.4 K in various applied magnetic fields. From the $\rho(T)$ measurements [see Fig. 7(b)], the applied magnetic field has been taken to be the H_{c2} for the temperature at which the resistance drops to zero.

The data for $H_{c2}(T)$ obtained from all the measurements are plotted in Fig. 12. In the temperature range of the SQUID magnetometer measurements (1.7–2.4 K), all the data match well and the temperature dependence of H_{c2} is linear. Close to T_c the slope of the $H_{c2}(T)$ curve is $\frac{dH_{c2}(T)}{dT} \sim -200$ Oe/K. However, there is an upward curvature at lower temperatures as seen in the $H_{c2}(T)$ data extracted from the ac $\chi(T)$ measurements. This upward curvature is sometimes seen in unconventional superconductors[27,28] and also in the multiband superconductor MgB$_2$.[29]

The temperature dependence of the change in London penetration depth, $\Delta\lambda(T)=\lambda(T)-\lambda(T_{min})=\lambda(T)-\lambda(0.52$ K$)$, is obtained from the $\chi(T)$ data at $H=0$ in Fig. 11 using Eq. (1). The result is shown in Fig. 13(a). The temperature dependence of the superfluid density $n_s(T)$ (the fraction of condensed electrons) can be obtained from the London penetration depth λ using the relation[30]

$$n_s = \left[\frac{\lambda(0)}{\lambda(T)}\right]^2. \qquad (14)$$

The n_s can be written in terms of the measured change in London penetration depth $\Delta\lambda(T)$ as

$$\Delta\lambda(T) = \lambda(T) - \lambda(0.52 \text{ K}) = \lambda(0)\left(\frac{1}{\sqrt{n_s}} - C\right), \qquad (15)$$

where $C=\lambda(0.52$ K$)/\lambda(0)$. The superfluid density depends on the shape of the Fermi surface and the superconducting gap symmetry. If we assume a spherical Fermi surface and s-wave superconductivity for OsB$_2$, n_s is just a function of temperature and the magnitude of the zero temperature su-
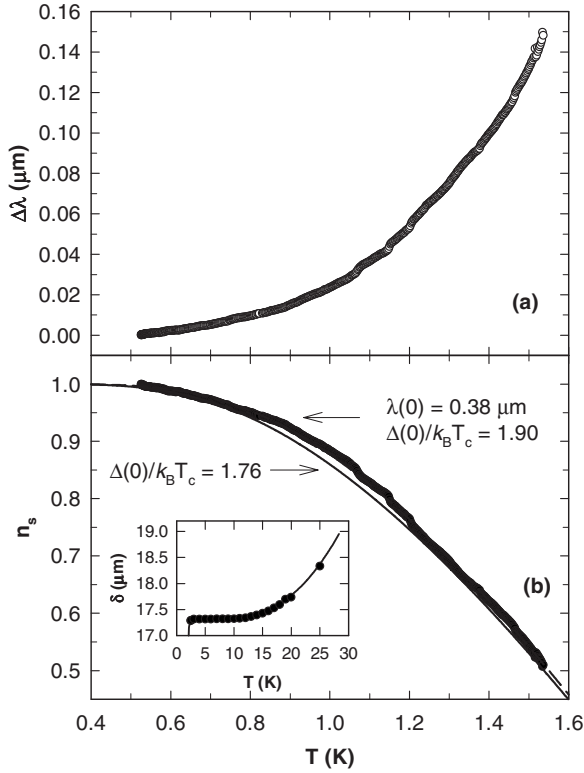
FIG. 13. (a) The temperature T dependence of the change $\Delta\lambda$ in penetration depth in zero magnetic field $\Delta\lambda(T) \equiv \lambda(T) - \lambda(0.52\ \text{K})$. (b) The temperature dependence of the superfluid density $n_s(T)$ of OsB_2. The solid circles are the data, the dashed line is a fit by the standard s-wave BCS model in the clean limit where the superconducting gap $\Delta(0)$ was allowed to vary, and the solid line is a fit by the standard s-wave BCS model in the clean limit, with the gap fixed to the weak-coupling BCS value $\Delta(0) = 1.76 k_B T_c$. The inset shows the calibrated normal-state skin depth (solid curve) compared to the data from resistivity measurements (solid circles).

perconducting gap $\Delta(0)$.[13] We fit the $\Delta\lambda(T)$ data shown in Fig. 13(a) using Eq. (15) with $\lambda(0)$, C, and $\Delta(0)$ the fitting parameters, where we use $T_c \equiv 2.15\ \text{K}$ and the clean limit BCS expression for $n_s(T, \Delta(0))$ within a semiclassical approximation.[31,32] The fit gave the value $\lambda(0) = 0.38(2)\ \mu\text{m}$, $C = 1.003(2)$, and a slightly enhanced value for the superconducting gap $\Delta(0) = 1.90(5) k_B T_c$. Allowing T_c to vary in the fit gave no significant change to the above initially assumed value of T_c. The $n_s(T)$ data obtained from the estimated value of $\lambda(0)$ and the measured $\Delta\lambda(T)$ using Eq. (14) are shown in Fig. 13(b). Figure 13(b) also shows the results of the full-temperature BCS calculations for a weak-coupling s-wave BCS model with a fixed gap $\Delta(0) = 1.76 k_B T_c$ (solid curve) and the result for an s-wave BCS model with the above gap $\Delta(0) = 1.90(5) k_B T_c$ (dashed curve). The observed behaviors of $\lambda(T)$ and $n_s(T)$ are consistent with s-wave superconductivity.

We now give a thermodynamic argument in favor of type-II superconductivity. The zero temperature thermodynamic critical field $H_c(0)$ of a superconductor is related to the zero temperature superconducting gap $\Delta(0)$ by the weak-coupling BCS expression[33]

$$\frac{H_c(0)^2}{8\pi} = \frac{N(\epsilon_F)(1 + \lambda_{\text{ep}})\Delta(0)^2}{4}, \quad (16)$$

where $N(\epsilon_F)$ is the density of states at the Fermi energy for both spin directions. The factor $(1 + \lambda_{\text{ep}})$ has been included on the right hand side of Eq. (16) to include effects of the renormalization of $N(\epsilon_F)$ due to the electron-phonon coupling. For OsB_2, from our experimental γ value and Eq. (12), one has $N(\epsilon_F)(1 + \lambda_{\text{ep}}) = 1.63$ states/eV f.u. $= 3.7 \times 10^{34}$ states/erg cm^3. Also, our penetration depth data gave $\Delta(0)/k_B T_c = 1.90$, which gives $\Delta(0) = 5.6 \times 10^{-16}$ erg. Therefore, Eq. (16) gives $H_c(0) = 270$ G. However, from Fig. 12, the $T = 0$ K critical field is $\geqslant 420$ Oe. Therefore, the critical field shown in Fig. 12 cannot be H_c, it must be H_{c2}, and therefore, OsB_2 is a type-II superconductor. The effect of stronger coupling is to reduce the calculated condensation energy[33] and give a smaller thermodynamic critical field, and so the argument above in favor of type-II superconductivity in OsB_2 holds regardless.

One can estimate the Ginzburg-Landau parameter κ using the relation[34]

$$H_{c2} = \sqrt{2}\kappa H_c. \quad (17)$$

With the value $H_c(0) = 270$ G obtained above and the value $H_{c2}(0) \geqslant H_{c2}(0.52\ \text{K}) = 420$ G, we get $\kappa(0) \geqslant 1.08$. This value of κ supports our above thermodynamic argument and puts OsB_2 on the type-II side of the borderline ($\kappa = 1/\sqrt{2}$) between type-I and type-II superconductivity.

The κ can also be estimated from the relation[34]

$$\kappa = \frac{\lambda}{\xi}. \quad (18)$$

For a type-II superconductor, the coherence length ξ can be estimated from the measured H_{c2} using the Ginzburg-Landau relation[34]

$$H_{c2} = \phi_0/2\pi\xi^2, \quad (19)$$

where $\phi_0 = hc/2e = 2.068 \times 10^{-7}$ G cm^2 is the flux quantum. Since we have $H_{c2}(T)$, we can get $\xi(T)$ using Eq. (19) and, hence, $\kappa(T) = \frac{\lambda(T)}{\xi(T)}$ from the measured $\lambda(T)$. The $\xi(T)$ and $\kappa(T)$ thus determined are shown in Fig. 14. Since the Ginzburg-Landau equations are written assuming a small order parameter, which means near T_c,[34] the dividing line between type-I and type-II superconductivity being $1/\sqrt{2}$ is defined near T_c. Therefore, our $\kappa(T)$ was fitted by a second order polynomial temperature dependence to get the extrapolated value $\kappa(T_c = 2.14\ \text{K}) = 2.41(3)$. This value of κ is larger compared to the estimate made above, but supports the type-II nature of superconductivity concluded above. It should be kept in mind that the above analysis was carried out assuming isotropic superconducting properties. Therefore, our values of λ, ξ, and κ for polycrystalline samples may need revision when single crystal measurements become available. In particular, the value of $\kappa(0.6\ \text{K}) \approx 4.2$ in Fig. 14 estimated using Eq. (18) and $H_{c2}(0.6\ \text{K}) \approx 420$ Oe from Fig. 12 lead to $H_c(0.6\ \text{K}) \approx 75$ Oe from Eq. (17), which is inconsistent with the value $H_c(0) = 270$ Oe estimated above from Eq. (16).
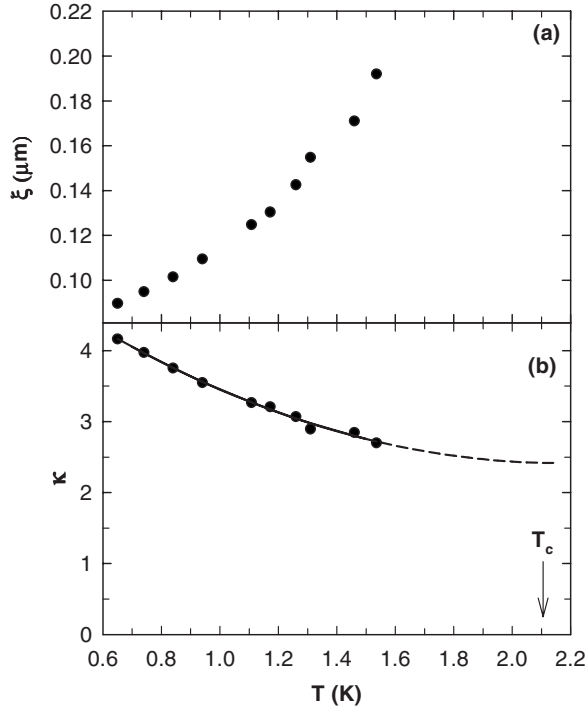
FIG. 14. (a) The temperature T dependence of the coherence length ξ and (b) of the Ginzburg-Landau parameter κ. The solid curve in (b) is a fit by a second order polynomial temperature dependence. The dashed line is an extrapolation up to T_c, which is shown as the vertical arrow.

This inconsistency may be associated with anisotropy effects.

If the mean free path l could be made larger by improving the quality of the sample, OsB_2 has the potential to be a nonelemental type-I superconductor. To this end, we have annealed a part of sample A and performed measurements on it. In the next section, we present our results on the annealed sample.

C. Annealed OsB_2 sample

The $\rho(T)$ data between 1.7 and 300 K are shown in Fig. 15. The room temperature value $\rho(300\ K)=36(3)\ \mu\Omega$ cm is the same as the value observed for the unannealed sample. The low-temperature residual resistivity $\rho_0=0.87(8)\ \mu\Omega$ cm (see inset in Fig. 15) is smaller than the value $1.7(2)\ \mu\Omega$ cm observed for the unannealed sample in the inset of Fig. 3. The residual resistivity ratio is 41 compared to the value of 22 for the unannealed sample. This indicates an improved sample quality with smaller amount of disorder. The inset in Fig. 15 shows the $\rho(T)$ data between 1.7 and 2.5 K measured with various applied magnetic fields. The abrupt drop to zero resistance at $T_c=2.12$ K seen for the zero-field data is suppressed to lower temperatures with increasing field.

The results of our magnetic measurements on the annealed OsB_2 sample are summarized in Fig. 16. In the $\chi_v(T)$ data shown in Fig. 16(a), a sharp steplike transition is seen at $T_c=2.1$ K compared to the relatively rounded transition for the unannealed sample in Fig. 8. The Meissner fraction (FC

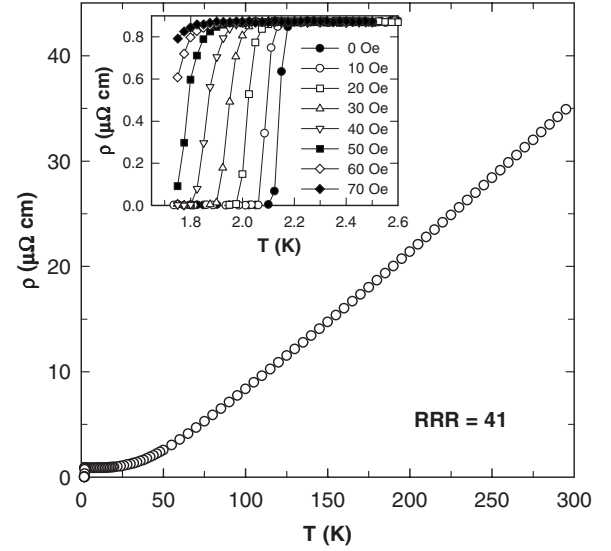FIG. 15. Electrical resistivity ρ versus temperature T for annealed OsB_2. The inset shows the low-temperature data measured in various applied magnetic fields.

data) has also increased in the annealed sample. Figure 16(b) shows the ZFC $\chi_v(T)$ data between 1.7 and 2.25 K measured in magnetic fields of 5–50 Oe in steps of 5 Oe. The superconducting transition is gradually suppressed to lower temperatures upon the application of higher magnetic fields. Figure 16(c) shows the hysteresis loop of the volume magnetization M_v versus magnetic field H at 1.75 K. The reversible part of the magnetization seems to have slightly increased as compared to the unannealed sample (see Fig. 10). Figure 16(d) shows the $M_v(H)$ data measured at various temperatures. The data are similar to those obtained for the unannealed sample.

The specific heat $C(T)$ data between 1.75 and 4 K measured in zero and 1 kOe applied magnetic field are shown in Fig. 17(a). A sharp steplike transition is seen at $T_c=2.13$ K compared to the broad peak for the unannealed sample (see Fig. 7). The 1 kOe data could be fitted by the expression $C(T)=\gamma T+\beta T^3$. The fit gave the values $\gamma=1.47(3)$ mJ/mol K^2 and $\beta=0.035(1)$ mJ/mol K^4. Using the above value of γ, one can estimate the density of states for both spin directions $N(\epsilon_F)$ from Eq. (12). One obtains $N(\epsilon_F)=0.88$ and 0.82 states/eV f.u. for $\lambda_{ep}=0.41$ and 0.5, respectively. These values are somewhat smaller than the above values obtained for the unannealed sample (1.14 and 1.06 states/eV f.u., respectively), but closer to the band structure value of 0.55 states/eV f.u.[9]

The inset in Fig. 17(a) shows the difference $\Delta C(T)$ between the zero field and 1 kOe data plotted as $\Delta C(T)/T$ versus T. From an equal entropy construction shown as the solid line in the inset, one gets $\Delta C/\gamma T_c=1.38$, which is close to the weak-coupling BCS value of 1.43. Figure 17(b) shows the specific heat data measured with various applied magnetic fields. The transition occurs at lower temperatures with increasing field. For magnetic fields above 20 Oe, the specific heat peaks at a larger value compared to the 0 and 10 Oe data before coming down to meet the zero-field data at
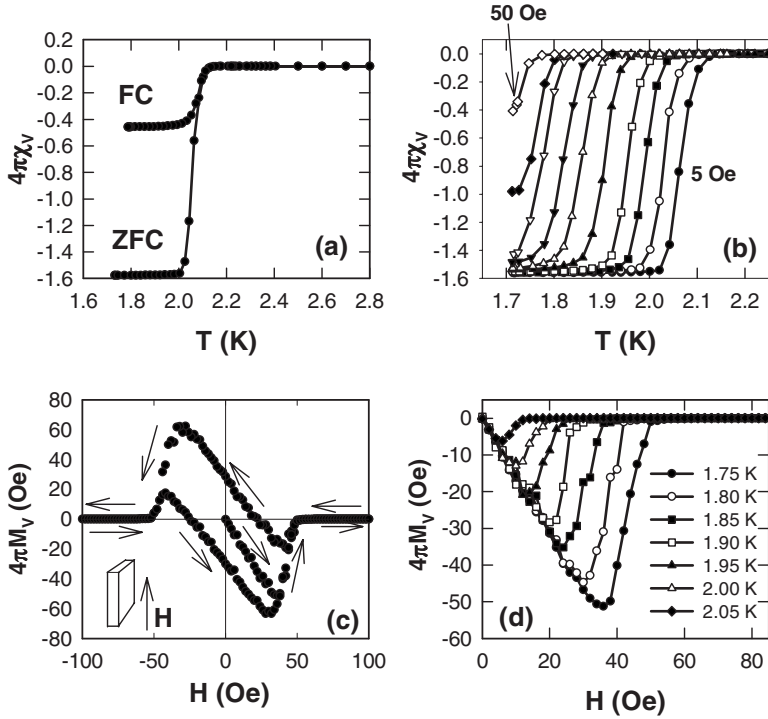
FIG. 16. (a) Temperature dependence of the ZFC and FC volume susceptibility $\chi_v(T)$ of annealed OsB_2, in a 5 Oe applied magnetic field, in terms of the volume fraction ($4\pi\chi_v$). (b) The temperature dependence of the zero-field-cooled volume susceptibility $4\pi\chi_v(T)$ measured in magnetic fields of 5–50 Oe in 5 Oe steps. (c) Hysteresis loop of the volume magnetization M_v normalized by $1/4\pi$, versus applied magnetic field H at 1.75 K. The magnetic field is applied parallel to the length of the sample as shown in the inset. The arrows next to the data show the direction of field ramping during the measurement. (d) Volume magnetization M_v versus applied magnetic field H at various temperatures.

lower temperatures. Measurements down to lower temperatures are required to see if this is a first order transition as seen in type-I superconductors as observed, for example, in Ir_2Ga_9.[35]

Figure 18 shows the results of our Hall effect measurements. Figure 18(a) shows the dependence of the Hall coefficient R_H on magnetic field H at various temperatures. The R_H is positive at all fields and temperatures, which indicates that hole conduction dominates the electronic transport. The R_H is approximately constant with magnetic field at all temperatures. From R_H, one obtains a lower limit estimate of the carrier density using the single-band expression[36]

$$R_H = \frac{1}{ne},$$

where n is the carrier density and e is the charge of the electron. Using the value $R_H = 2.03 \times 10^{-4}$ cm^{-3} C^{-1} at 300 K and 8 T, we get $n = 3.08 \times 10^{22}$ cm^{-3}. One can get an estimate of the density of states at the Fermi energy $N(\epsilon_F)$ using the single-band relation[22]

$$N(\epsilon_F) = \left[\frac{m(3\pi^2 n)^{1/3}}{\hbar^2 \pi^2} \right], \tag{20}$$

where m is the free electron mass and $\hbar$ is Planck's constant divided by 2π. With the value of n obtained above, one gets $N(\epsilon_F) = 0.71$ states/eV f.u. for both spin directions, which is close to the range 0.81–0.88 states/eV f.u. obtained above from the heat capacity for the annealed sample. This agreement suggests that the carrier density estimated from the Hall measurements may not be far off from the actual value for the material.

Figure 18(b) shows the plot of R_H versus temperature T, and the inset shows the variation of the carrier density n with
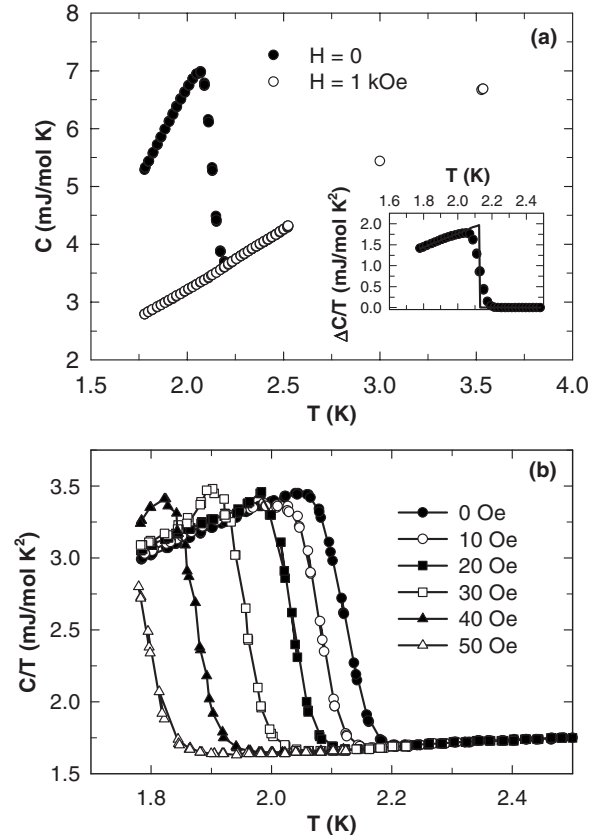

FIG. 17. (a) Temperature dependence of the heat capacity $C(T)$ of annealed OsB_2 in zero and 1 kOe applied magnetic field. The inset shows the difference $\Delta C(T)$ between the two data sets plotted as $\Delta C/T$ versus T. The solid line in the inset is an equal entropy construction to estimate the magnitude of the superconducting anomaly (see text for details). (b) C/T versus T between 1.75 and 2.5 K measured with various applied magnetic fields.
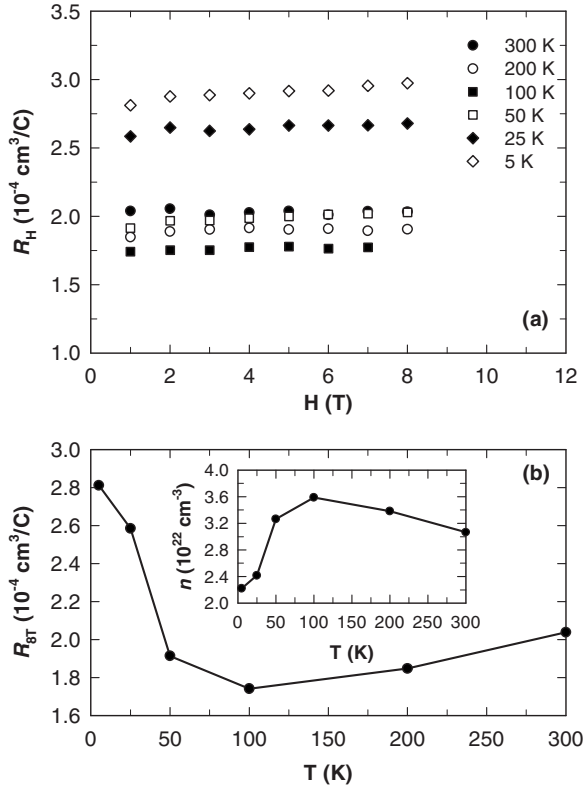
FIG. 18. (a) The Hall coefficient R_H versus magnetic field H measured at various temperatures. (b) The Hall coefficient R_H versus temperature T in a magnetic field of 8 T. The inset in (b) shows the inferred variation of the carrier density n with temperature T in a single-band model.

FIG. 19. Dynamic susceptibility χ of annealed OsB_2 normalized by $1/4\pi$, versus temperature T at a frequency of 10 MHz in various applied magnetic fields H. The H values in Oe are given next to the data. The data have been normalized to a minimum value of -1 at the lowest T. For comparison, the $H=0$ Oe data for the unannealed sample are shown as solid symbols.

T at a magnetic field of 8 T. R_H shows a strong temperature dependence, decreasing slightly for temperatures down to 50 K before increasing strongly at lower temperatures. In a single-band model, the R_H is expected to be temperature independent if the scattering rate τ is isotropic. However, in a two-band model, R_H could be temperature dependent if, for example, the scattering rates of the two bands have a different temperature dependence or the fractions of charge carriers in the two bands change with temperature.[36] The strong reduction in n below 50 K mimics the behavior observed for the instrinsic susceptibility shown above in Fig. 5.

We now present the results of the dynamic susceptibility measurements on the annealed sample. Figure 19 shows the dynamic susceptibility χ of annealed OsB_2 normalized by $1/4\pi$, versus temperature T at a frequency of 10 MHz in various applied magnetic fields H. The zero-field data for the unannealed sample are also shown for comparison. The data have been normalized to a minimum value of -1 at the lowest T. The steplike feature at 1.6 K seen for the unannealed sample is no longer observed for the annealed sample, suggesting an improved sample quality. The critical field $H_{c2}(T)$ was obtained from the $\chi(T)$ data shown in Fig. 19 for the data measured in magnetic fields up to $H=335$ Oe for the annealed sample as described in Sec. III B 2 for the unannealed sample. The $H_{c2}(T)$ data so obtained are plotted in Fig. 20 along with the $H_{c2}(T)$ data extracted from the $\chi(T)$
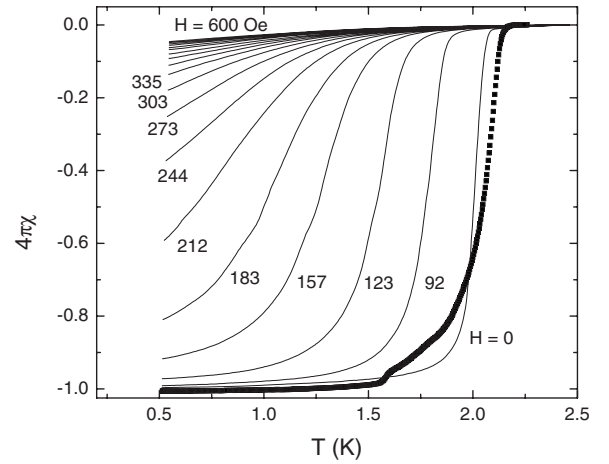
data in Fig. 16(b), the $\rho(T)$ data in the inset of Fig. 15, the $M(H)$ data in Fig. 16(d), and the $C(T)$ data in Fig. 17(b). The $H_{c2}(T)$ data between 1.7 and 2.2 K are linear with $\frac{dH_{c2}(T)}{dT}$ ~ -180 Oe/K near T_c. The data at lower temperatures show a positive curvature similar to that seen for the unannealed sample in Fig. 12 above.

The temperature dependence of the change in London penetration depth, $\Delta\lambda(T) = \lambda(T) - \lambda(T_{\min}) = \lambda(T) - \lambda(0.52 \text{ K})$, is obtained from the $\chi(T)$ data at $H=0$ in Fig. 19 using Eq. (1). The result is shown in Fig. 21(a). The smoothly varying $\chi(T)$ data up to T_c allowed us to analyze the data to much higher temperatures than was possible for the unannealed sample, which showed an unexpected bump at about 1.6 K. As described in detail in Sec. III B 2, we obtain the superfluid density $n_s(T)$ data by fitting the $\Delta\lambda(T)$ data shown in Fig. 21(a) using Eq. (15) with $\lambda(0)$, C, and $\Delta(0)$ the fitting parameters.
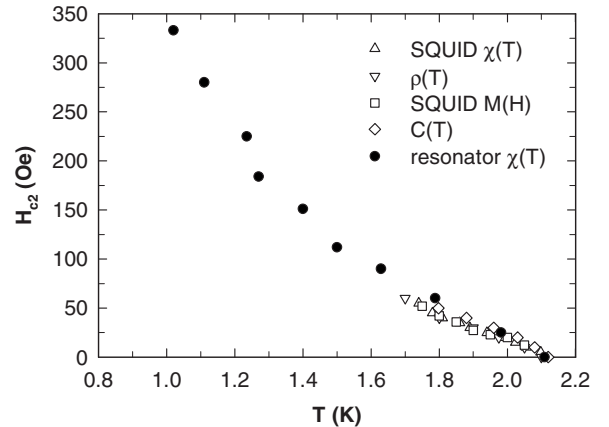

FIG. 20. Critical magnetic field H_{c2} versus temperature T for annealed OsB_2 extracted from various measurements as noted.
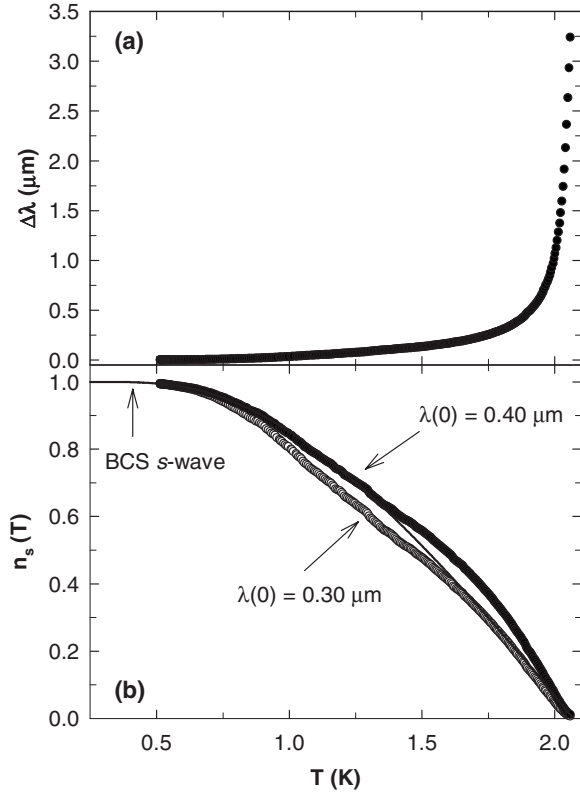
FIG. 21. (a) The temperature T dependence of the change $\Delta\lambda$ in penetration depth of annealed OsB_2 in zero magnetic field $\Delta\lambda(T)$ $\equiv \lambda(T)-\lambda(0.52$ K$)$. (b) The temperature dependence of the super-fluid density $n_s(T)$ of annealed OsB_2. The filled circles are the data with $\lambda(0)=0.40$ μm, and the open circles are the data with $\lambda(0)$ $=0.30$ μm. The solid line is the standard weak-coupling s-wave BCS model in the clean limit.

The $\Delta\lambda(T)$ data could not be fitted in the whole temperature range with the clean limit BCS model with a single $\lambda(0)$ value if we assume that there is only one gap. With a single weak-coupling s-wave BCS gap $\Delta(0)/k_BT_c=1.76$, fitting the data between 0.52 and 1.3 K gave $\lambda(0)=0.40$ μm, and fitting the data above 1.6 K gave $\lambda(0)=0.30$ μm. The superfluid density $n_s(T)$ data thus obtained for the two values of $\lambda(0)$ mentioned above are shown in Fig. 21(b) along with the prediction of the weak-coupling s-wave BCS model shown as the solid curve. The $n_s(T)$ data have an unusual temperature dependence with two bumps at about 0.8 and 1.7 K. This is very similar to the behavior of $n_s(T)$ seen in polycrystalline and single crystalline MgB_2.[37]

We were indeed able to fit our $n_s(T)$ data with a two-gap model using the dirty limit expression[38]

$$n_s(T) = a\frac{\Delta_1(T)\tanh\left(\dfrac{\Delta_1(T)}{2k_BT_c}\right)}{\Delta_1(0)} + b\frac{\Delta_2(T)\tanh\left(\dfrac{\Delta_2(T)}{2k_BT_c}\right)}{\Delta_2(0)},$$

(21)

where $\Delta_1(T)$ and $\Delta_2(T)$ are the temperature dependent gaps, $\Delta_1(0)$ and $\Delta_2(0)$ are the zero temperature values of the gaps,
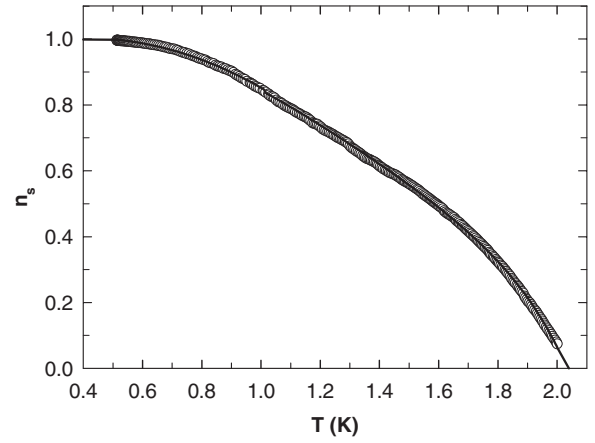

FIG. 22. The temperature dependence of the superfluid density $n_s(T)$ of annealed OsB_2 for $\lambda(0)=0.40$ μm. The solid line is a fit by a two-gap model in the dirty limit given by Eq. (21).

and a and b are the fractional contributions from bands 1 and 2, respectively. The temperature dependence of the gap is given by $\Delta(T)=\Delta(0)\tanh(c\sqrt{T_c/T-1})$, where c is a parameter which depends on the symmetry of the superconducting gap.[39] The fit shown in Fig. 22 as the solid line through the $n_s(T)$ data gave the values $2\Delta_1(0)/k_BT_c=2.8(3)$, $2\Delta_2(0)/k_BT_c=3.6(4)$, $a=0.22(3)$, $b=0.85(4)$, and $c=3.8(2)$. The two-gap model fits the data very well. We could also fit the $n_s(T)$ data with a two-gap model when the critical temperature T_c for the two gaps were allowed to vary. The fit (not shown here) gave a slightly smaller value for the smaller gap $2\Delta_1(0)/k_BT_c=2.2(1)$ and gave a $T_c=1.5(2)$ K for this gap. The other parameters did not change much. The similar values of $\Delta_1(0)$ and $\Delta_2(0)$ may be the reason why the specific heat jump at T_c is close to the value expected for a single weak-coupling BCS gap.

We point out that for the unannealed sample, due to the step in the $\chi(T)$ at about 1.6 K, the $n_s(T)$ data in Fig. 13 were fitted only up to 1.5 K. Therefore, we do not know whether the $n_s(T)$ data for the unannealed sample in the absence of this feature would be described by the BCS model in the whole temperature range up to T_c. In our model, we assume an isotropic gap. The deviation from the theory in Fig. 21 could come from anisotropy of the gap or due to multiband effects such as in MgB_2.[37] Measurements on single crystals will be needed to resolve this issue.

Using the values $\Delta(0)=1.76k_BT_c=5.2\times10^{-16}$ erg and $N(\epsilon_F)=0.88$ states/eV f.u.$=2\times10^{34}$ states/erg cm^3 obtained from the specific heat data, one gets from Eq. (16) $H_c(0)$ $=190$ G. The critical field for the annealed sample at 1.0 K in Fig. 20 is already about 350 G. Therefore, annealed OsB_2 is still a type-II superconductor. An estimate of the Ginzburg-Landau parameter κ can now be made using Eq. (17). With the value $H_c(0)=190$ G obtained above and the value $H_{c2}(0)\geq H_{c2}(1$ K$)=335$ G, we get $\kappa(0)\geq1.2$, indicating the type-II nature of the superconductivity of the annealed sample.
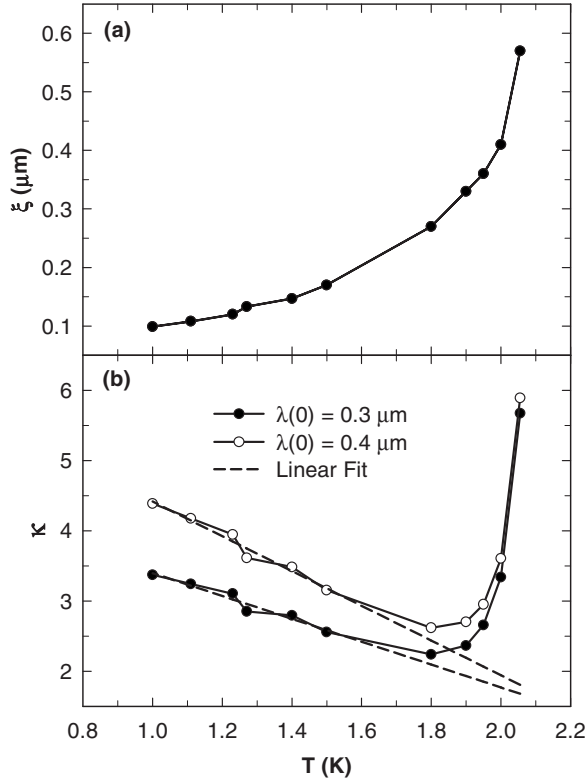
FIG. 23. (a) The temperature T dependence of the coherence length ξ for annealed OsB_2 and (b) of the Ginzburg-Landau parameter κ for annealed OsB_2 for $\lambda(0)=0.3$ and 0.4 μm. The solid curves through the data are guides for the eye. The dashed curves in (b) are linear fits to the $\kappa(T)$ data between 1.0 and 1.5 K and extrapolated to T_c.

From the $H_{c2}(T)$ data in Fig. 20, we can get $\xi(T)$ using Eq. (19), and from Eq. (18), we can get $\kappa(T)$ using the $\Delta\lambda(T)$ data in Fig. 21(a), with $\lambda(0)=0.3$ or 0.4 μm obtained above. The $\xi(T)$ and $\kappa(T)$ data thus obtained are plotted in Figs. 23(a) and 23(b), respectively. The behavior of $\kappa(T)$ near T_c is unusual. Such a behavior has been reported before for small spheres of the type-I superconductors tin and indium,[40] where it was suggested that the divergence of the measured κ near T_c comes from finite size effects; near T_c when the coherence length and penetration depth become comparable to the size of the sample, the apparent κ diverges. A similar increase of κ near T_c has also been reported recently for single crystals of the type-I superconductor $Ag_5Pb_2O_6$.[41] Divergence of several quantities including κ near T_c has also been reported in high-T_c materials, and this behavior was shown to arise from the interaction of vortices near T_c, where the size of the vortices became comparable to the distance between the vortices.[42] The reason for such a behavior for OsB_2 is unclear, and further measurements will be required to understand this issue. To get an alternative estimate of κ near T_c, we have fitted the $\kappa(T)$ data between 1.0 and 1.5 K and extrapolated to T_c. The fits, shown as the dashed straight lines through the data in Fig. 23, gave the values $\kappa(T_c)$ = 1.80 and 1.63 for $\lambda(0)=0.4$ and 0.3 μm, respectively.

Another estimate of κ can be made as follows. First, the residual resistivity $\rho_0=0.87$ $\mu\Omega$ cm (see inset in Fig. 15) gives the mean free path $l=mv_F/\rho_0ne^2=0.084$ μm, where m is taken to be the free electron mass, v_F is the Fermi velocity, n is the conduction electron density, and e is the electron charge. Using the value $n=3.08\times10^{22}$ cm^{-3} obtained from the Hall effect measurements, in a single-band model, one has[22] $v_F=\left(\frac{h}{2\pi m}\right)(3\pi^2n)^{2/3}\approx5.9\times10^7$ cm/s. The BCS coherence length is then[34] $\xi_0=\hbar v_F/\pi\Delta(0)\simeq0.38$ μm. Since ξ_0 is larger than l, annealed OsB_2 is not in the clean limit. The effective coherence length is then[34] $\xi(0)=0.85\sqrt{\xi_0 l}$ $=0.151$ μm, and the Ginzburg-Landau parameter κ can be estimated using Eq. (18). We get $\kappa(0)=1.99$ and 2.6 for $\lambda(0)=0.30$ and 0.40 μm, respectively. These values of κ are consistent with the value $\kappa(0)\geqslant1.2$ obtained from the thermodynamic argument above, and also with the $\kappa(T)$ values obtained from linear fits to the $\kappa(T)$ data above. These values support our conclusion that OsB_2 is a type-II superconductor.

IV. CONCLUSION

We have synthesized the compounds OsB_2 and RuB_2, and measured their magnetic, transport, and thermal properties. Our measurements confirm that OsB_2 undergoes a bulk transition into the superconducting state below 2.1 K. Analysis of our data suggests that OsB_2 is a moderate-coupling (λ_{ep} $=0.4-0.5$) type-II superconductor with a small Ginzburg-Landau parameter $\kappa\sim1-2$ and an upper critical field $H_{c2}(0.5$ K$)\sim420$ Oe for an unannealed sample and $H_{c2}(1$ K$)\sim330$ Oe for an annealed sample. The reduced specific heat jump at T_c observed for the unannealed sample and the positive curvature in $H_{c2}(T)$ observed for both the unannealed and annealed samples are similar to effects observed in MgB_2. The temperature dependence of the superfluid density $n_s(T)$ is consistent with an s-wave superconductor with a slightly enhanced gap $\Delta(0)=1.90(5)k_BT_c$ and a zero temperature London penetration depth $\lambda(0)=0.38(2)$ μm for the unannealed OsB_2 sample, and $\Delta(0)=1.76k_BT_c$ and $\lambda(0)$ $=0.30-0.40$ μm for the annealed OsB_2 sample. For the annealed sample, the $n_s(T)$ data above 1.4 K deviate from the predictions of the s-wave BCS model and show a shoulder at 1.8 K. This behavior is similar to the behavior observed in MgB_2. In the normal state, unannealed OsB_2 and RuB_2 are Pauli paramagnetic metals with very similar properties. To investigate the effect of boron off-stoichiometry on the superconducting properties of OsB_2, we also investigated samples with starting compositions $OsB_{1.9}$ and $OsB_{2.1}$. Both samples had a transition temperature $T_c=2.1$ K, indicating no significant dependence of T_c on the boron stoichiometry. The diminished specific heat jump at T_c in Fig. 7(b) for the unannealed sample, the non-type-II shape of the superconducting $M(H)$ in Figs. 9 and 16(d), the positive curvature in $H_{c2}(T)$ in Figs. 12 and 20, and the non-BCS-like temperature dependence of the $n_s(T)$ in Fig. 21(b) are all interesting issues that require further investigation. Future studies of the anisotropic physical properties of single crystals will be very helpful in these regards.

[1] J. Nagamastu, N. Nakagawa, T. Muranaka, Y. Zenitani, and J. Akimitsu, Nature (London) **410**, 63 (2001).

[2] D. Kaczorowski, A. J. Zaleski, O. J. Zogal, and J. Klamut, arXiv:cond-mat/0103571 (unpublished).

[3] V. A. Gasparov, N. S. Sidorov, I. I. Zverkova, and M. P. Kulakov, JETP Lett. **73**, 532 (2001).

[4] H. Rosner, W. E. Pickett, S.-L. Drechsler, A. Handstein, G. Behr, G. Fuchs, K. Nenkov, K.-H. Muller, and H. Eschrig, Phys. Rev. B **64**, 144516 (2001).

[5] A. S. Cooper, E. Corenzwit, L. D. Longinotti, B. T. Matthias, and W. H. Zachariasen, Proc. Natl. Acad. Sci. U.S.A. **67**, 313 (1970).

[6] N. I. Medvedeva, A. L. Ivanovskii, J. E. Medvedeva, and A. J. Freeman, Phys. Rev. B **64**, 020502(R) (2001).

[7] J. M. Vandenberg, B. T. Matthias, E. Corenzwit, and H. Barz, Mater. Res. Bull. **10**, 889 (1975).

[8] R. W. Cumberland, M. B. Weinberger, J. J. Gilman, S. M. Clark, S. H. Tolbert, and R. B. Kaner, J. Am. Chem. Soc. **127**, 7264 (2005).

[9] M. Hebbachea, L. Stuparevi, and D. Zivkovi, Solid State Commun. **139**, 227 (2006).

[10] Z. Y. Chen, H. J. Xiang, J. Yang, J. G. Hou, and Q. Zhu, Phys. Rev. B **74**, 012102 (2006).

[11] L. Stuparevic and D. Zivkovic, J. Therm Anal. Calorim. **76**, 975 (2004).

[12] B. J. Suh, X. Zong, Y. Singh, A. Niazi, and D. C. Johnston, Phys. Rev. B **76**, 144511 (2007).

[13] For a topical review, see R. Prozorov and R. W. Giannetta, Supercond. Sci. Technol. **19**, R41 (2006).

[14] R. Prozorov, R. W. Giannetta, A. Carrington, P. Fournier, R. L. Greene, P. Guptasarma, D. G. Hinks, and A. R. Banks, Appl. Phys. Lett. **77**, 4202 (2000).

[15] R. Prozorov, R. W. Giannetta, A. Carrington, and F. M. Araujo-Moreira, Phys. Rev. B **62**, 115 (2000).

[16] R. A. Young, Rietveld analysis program DBWS-9807A, Release 27.02.99, 1998.

[17] R. B. Roof, Jr. and C. P. Kempter, J. Chem. Phys. **37**, 1473 (1962).

[18] R. E. Peierls, *Quantum Theory of Solids* (Clarendon, Oxford, 1955).

[19] R. D. Shannon, Acta Crystallogr., Sect. A: Cryst. Phys., Diffr., Theor. Gen. Crystallogr. **A32**, 751 (1976).

[20] S. Chiodo, H. J. Gotsis, N. Russo, and E. Sicilia, Chem. Phys. Lett. **425**, 311 (2006).

[21] L. B. Mendelsohn and F. Biggs, Phys. Rev. A **2**, 1130 (1970).

[22] C. Kittel, *Solid State Physics* (Wiley, New York, 1966).

[23] S. L. Budko, G. Lapertot, C. Petrovic, C. E. Cunningham, N. Anderson, and P. C. Canfield, Phys. Rev. Lett. **86**, 1877 (2001).

[24] W. L. McMillan, Phys. Rev. **167**, 331 (1967).

[25] W. E. Pickett, Braz. J. Phys. **33**, 695 (2003).

[26] E. H. Brandt, Phys. Rev. B **68**, 054506 (2003).

[27] V. N. Zavaritsky, V. V. Kabanov, and A. S. Alexandrov, Europhys. Lett. **60**, 127 (2002).

[28] M. B. Maple, M. C. de Andrade, J. Herrmann, R. P. Dickey, N. R. Dilley, and S. Han, J. Alloys Compd. **250**, 585 (1997).

[29] Z. X. Shi, M. Tokunaga, T. Tamegai, Y. Takano, K. Togano, H. Kito, and H. Ihara, Phys. Rev. B **68**, 104513 (2003).

[30] C. J. Gorter and H. Casimir, Physica (Utrecht) **1**, 306 (1934).

[31] B. S. Chandrasekhar and D. Einzel, Ann. Phys. **2**, 535 (1993).

[32] R. Prozorov, T. A. Olheiser, R. W. Giannetta, K. Uozato, and T. Tamegai, Phys. Rev. B **73**, 184523 (2006).

[33] D. J. Scalpino, in *Superconductivity*, edited by R. D. Parks (Dekker, New York, 1969), Vol. 1, pp. 503, 536, and 537.

[34] M. Tinkham, *Introduction to Superconductivity* (McGraw-Hill, New York, 1975).

[35] T. Shibayama, M. Nohara, H. Aruga Katori, Y. Okamoto, Z. Hiroi, and H. Takagi, J. Phys. Soc. Jpn. **76**, 073708 (2007).

[36] C. M. Hurd, *The Hall Effect in Metals and Alloys* (Plenum, New York, 1972).

[37] F. Manzano, A. Carrington, N. E. Hussey, S. Lee, A. Yamamoto, and S. Tajima, Phys. Rev. Lett. **88**, 047002 (2002).

[38] A. Gurevich, Phys. Rev. B **67**, 184515 (2003).

[39] Charles P. Poole, Jr., Horacio A. Farach, Richard J. Creswick, and R. Prozorov, *Superconductivity*, 2nd ed. (Academic, The Netherlands, 2007).

[40] J. Feder and D. S. McLaughlin, Phys. Rev. **177**, 763 (1969).

[41] S. Yonezawa and Y. Maeno, Phys. Rev. B **72**, 180504(R) (2005).

[42] V. G. Kogan, M. Ledvij, A. Yu. Simonov, J. H. Cho, and D. C. Johnston, Phys. Rev. Lett. **70**, 1870 (1993).